Supplementary Information Document:
Numerical study of the effect of sidewalls on shock train behaviour

Alexander Gillespie[1,2*] and Neil D. Sandham[1]

[1]Aerodynamics and Flight Mechanics Group, University of Southampton, Southampton, UK, SO17 7PX
[2]Platform Systems Division, DSTL Portsdown West, Fareham, UK, PO17 6AD
*Corresponding author. E-mail: agillespie@dstl.gov.uk

Grid Refinement Study

In this grid study we discuss the sensitivity of the shock train flow properties to the mesh spacing. Here we compare two grid resolutions (denoted 'Baseline' and 'Fine'), with details listed in table 1. The fine grid has twice the resolution in the streamwise and spanwise directions and 50% more in the wall-normal resolution. The reported viscous grid spacing values correspond to boundary layer conditions at $x = 6h$ and, were it not for the need to capture shock waves and shock-induced separation, both grids would be considered as satisfying the usual conditions for direct numerical simulation (DNS). All grid cases are run at the stated flow conditions in the previous section and use the shorter $l_x = 16h$ configuration.

Table 1: Summary of grid resolutions upstream of the shock train ($x = 6h$).

Grid	N_x	N_y	N_z	Δx^+	Δy^+ (min/max)	Δz^+
Baseline	800	320	60	9.0	0.8/5	8.0
Fine	1600	480	120	4.5	0.5/4.0	4.0

Firstly, we assess the grid sensitivity of the boundary layer properties. For this, two cases were run with no applied back pressure and therefore no shock train occurring in the domain. For both cases the results discussed here represent the converged state of the boundary layer and the sampling time for statistics is $64h/u_1$ (roughly four full convective cycles through the computational domain if we assume an average convection velocity of $\bar{u} \sim u_1$).

In figure 1 we compare streamwise distributions of time- and span-averaged flow properties. There is a development region shortly downstream of the inlet (present in each of the charts) which illustrates the change from synthetic inflow to naturally-sustained turbulence. The natural growth of the boundary layer thickness (figures 1a and 1b) increases the confinement ratio in the channel, leading to an increase in wall pressure by roughly 18% (figure 1c). The presence of inflow compression waves is seen in the two spikes/dips in the wall pressure distribution at $x/h = 6$. These compression waves are weak and the flow recovers downstream, suggesting that the permanent effect of these waves can be neglected.

Skin friction provides information about the state of the boundary layer flow very close to the wall. The distribution of skin friction in figure 1d shows a very large variation in this development region, a feature which is common for these synthetic turbulence methods. After approximately $x = 6h$ the

distributions converge to constant slopes, suggesting that this is the length of the development region. The skin friction distribution shows the largest discrepancy between the two grid resolutions. The baseline case underestimates C_f by approximately 5% after the development region. The associated underestimation of displacement thickness (i.e. boundary layer blockage) at the baseline resolution leads to a 2% lower prediction of wall pressure near the end of the domain.

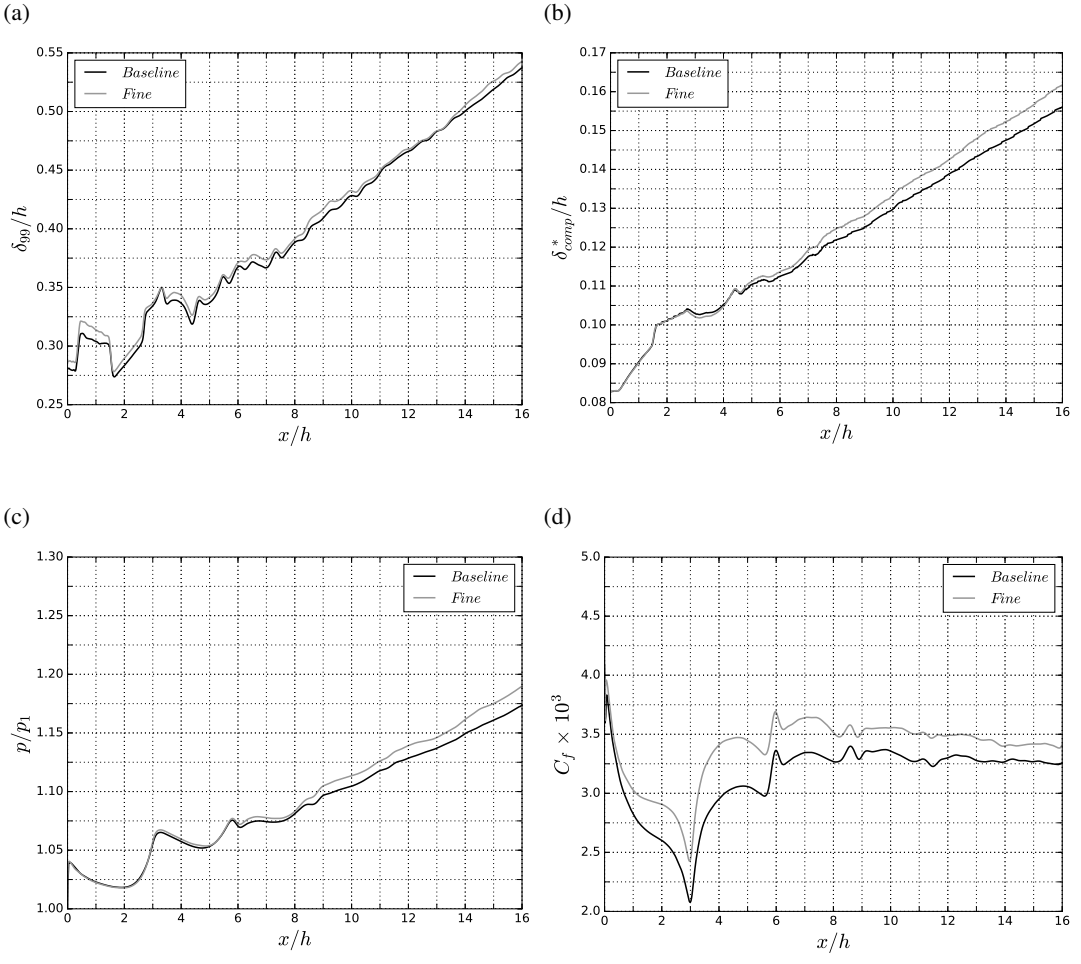

Figure 1: Grid resolution comparison of streamwise distributions of (a) 99% boundary layer thickness, (b) displacement thickness, (c) wall static pressure and (d) skin friction coefficient. The end of the boundary layer development region is estimated to occur where the skin friction stabilises at $x = 6h$.

Boundary layer profiles of velocity and Reynolds stresses at the end of the development region are shown in figure 2. In 2a we plot the van Driest-transformed velocity profile (see Huang and Coleman, 1994). Additional lines are provided for the $u^+ = y^+$ relation expected near the wall and the empirical logarithmic law of the wall. For both grid resolutions, the boundary layer edge values of $U^+_{vd,e} \sim 20$ are similar to other simulations of low Re, $M_1 = 2$ turbulent boundary layers (e.g. Wenzel et al., 2018). The overestimation of the U^+_{vd} distribution for the baseline grid is consistent with the lower skin friction seen previously and this overestimation is preserved further downstream. The stress profiles in figure 2b have been scaled by the density parameter $\xi = (\rho(y)/\rho_w)^{1/2}$ (Morkovin scaling – see Morkovin and

Favre, 1962; Wenzel et al., 2019). The change in grid resolution causes small differences (around 5%) in the turbulent stresses. The streamwise fluctuations of the baseline grid case are slightly overestimated, while the wall-normal and spanwise fluctuations are consistently underestimated.

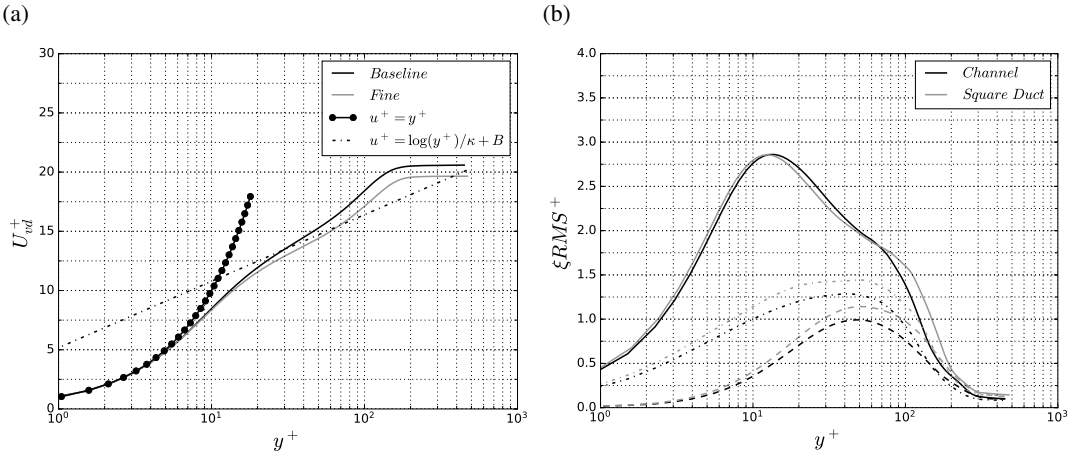

Figure 2: Grid resolution comparison of (a) van Driest-transformed velocity profile and (b) density-weighted Reynolds stress profiles (solid, dashed and dotted lines are respectively RMS of u', v' and w'). All profiles are taken at $x = 6h$.

To analyse the grid sensitivity of the shock train problem we apply a pressure ratio of 3.0 to the same numerical domain. For each grid, the simulation is initialised with a converged boundary layer profile. The simulation runs for $128h/u_1$ time units to allow the shock train to develop. The statistics are then captured over a a period of $64h/u_1$. The streamwise distribution of pressure at the wall and at the centreline is shown in figure 3. As is typical for shock trains, the wall pressure (figure 3a) rises gradually from the leading edge of the shock train to the outlet, whereas the centreline pressure (figure 3b) oscillates significantly through the compression and expansion regions of the shock train. The main effect of the grid resolution is to change the leading edge position of the shock train. The fine grid case has a shock train which is approximately $0.65h$ further upstream than the baseline case. This effect can be attributed to the difference in skin friction which has been shown to strongly affect the equilibrium position.

In figure 4 we account for the downstream shift in the shock train by plotting the pressure distributions aligned by the location of the leading shock (x_3). Here, the two sets of curves collapse well, up to the fourth shock cycle. This suggests that the baseline grid is able to reliably predict the effects of the boundary layers on the shock train structure, including the strength and spacing of the shock waves and this grid is employed for the remaining cases discussed in the current work.

References

Huang, P. G. and Coleman, G. N. (1994). Van Driest transformation and compressible wall-bounded flows. *AIAA Journal*, 32(10):2110–2113.

Morkovin, M. and Favre, A. (1962). Effects of compressibility on turbulent flows. In *Mécanique de la Turbulence*, pages 367–380. CNRS, Paris.

Wenzel, C., Gibis, T., Kloker, M., and Rist, U. (2019). Self-similar compressible turbulent boundary layers with pressure gradients. Part 1. Direct numerical simulation and assessment of morkovin's hypothesis. *Journal of Fluid Mechanics*, 880:239–283.

Wenzel, C., Selent, B., Kloker, M., and Rist, U. (2018). DNS of compressible turbulent boundary layers and assessment of data/scaling-law quality. *Journal of Fluid Mechanics*, 842:428–468.

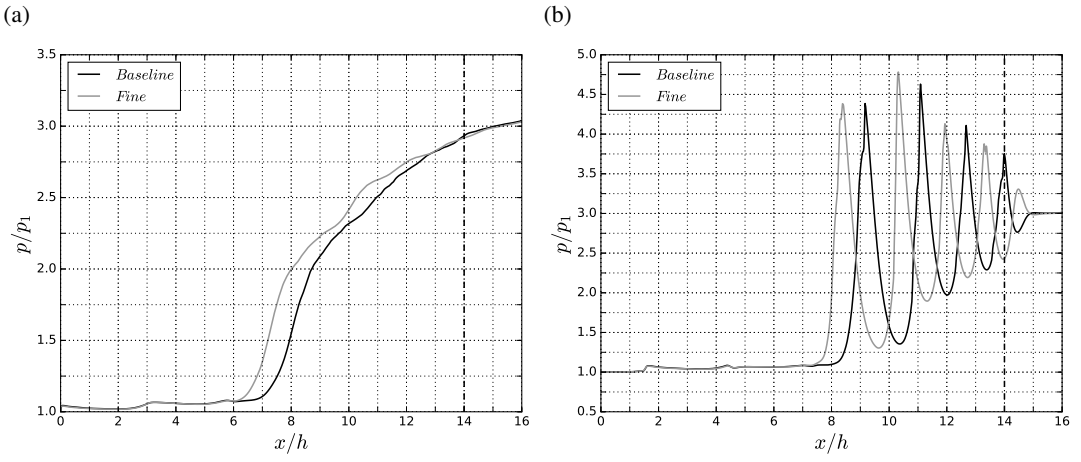

Figure 3: Streamwise distribution of pressure (a) at the wall and (b) at the centreline.

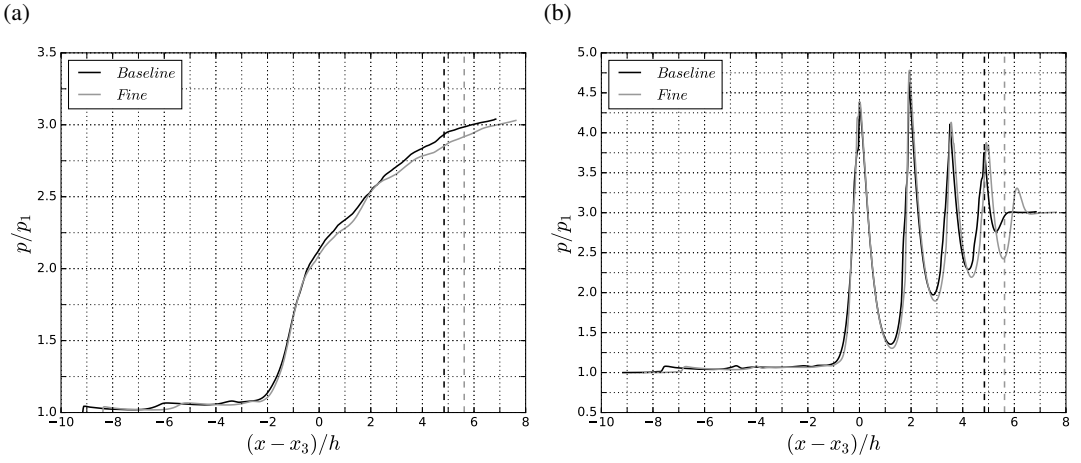

Figure 4: Adjusted distributions of (a) wall pressure and (b) centreline pressure. Aligning the location of the leading shock allows the profiles to collapse together very well.